Computer Vision and Image Understanding 201 (2020) 103075

Contents lists available at ScienceDirect

Computer Vision and Image Understanding

journal homepage: www.elsevier.com/locate/cviu

Accurate MR image super-resolution via lightweight lateral inhibition network

Xiaole Zhao [a], Xiafei Hu [b], Ying Liao [b], Tian He [b], Tao Zhang [b,c,d,*], Xueming Zou [b], Jinsha Tian [a]

[a] School of Computer Science and Technology, Southwest University of Science and Technology, Mianyang, China
[b] School of Life Science and Technology, University of Electronic Science and Technology of China (UESTC), Chengdu, China
[c] High Field Magnetic Resonance Brain Imaging Laboratory of Sichuan, Chengdu, China
[d] Key Laboratory for NeuroInformation of Ministry of Education, Chengdu, China

ARTICLE INFO

Keywords:
Convolutional neural network
Deep learning
Lateral inhibition
Magnetic resonance imaging
Super-resolution

ABSTRACT

In recent years, convolutional neural networks (CNNs) have shown their advantages on MR image super-resolution (SR) tasks. Many current SR models, however, have heavy demands on computation and memory, which are not friendly to magnetic resonance imaging (MRI) where computing resource is usually constrained. On the other hand, a basic consideration in most MRI experiments is how to reduce scanning time to improve patient comfort and reduce motion artifacts. In this work, we ease the problem by presenting an effective and lightweight model that supports fast training and accurate SR inference. The proposed network is inspired by the lateral inhibition mechanism, which assumes that there exist inhibitory effects between adjacent neurons. The backbone of our network consists of several lateral inhibition blocks, where the inhibitory effect is explicitly implemented by a battery of cascaded local inhibition units. When model scale is small, explicitly inhibiting feature activations is expected to further explore model representational capacity. For more effective feature extraction, several parallel dilated convolutions are also used to extract shallow features directly from the input image. Extensive experiments on typical MR images demonstrate that our lateral inhibition network (LIN) achieves better SR performance than other lightweight models with similar model scale.

1. Introduction

Magnetic resonance imaging (MRI) is a commonly-used and versatile non-invasive imaging modality with the advantages of multi-contrast and no ionizing radiation etc. Spatial resolution is one of the most important imaging parameters in most MRI experiments. In general, high-resolution (HR) images usually provide rich structural details and benefit more accurate image postprocessing, hence promoting effective subsequent analysis and early clinic diagnosis (Greenspan et al., 2001, 2002; Reeth et al., 2012; Shi et al., 2019). However, the spatial resolution of magnetic resonance (MR) images are typically constrained by various physical and physiological limitations, e.g., hardware device, imaging time, signal-to-noise ratio (SNR), and motion artifacts etc. (Reeth et al., 2012; Plenge et al., 2012). Increasing the spatial resolution of MR images typically reduces SNR, and increase imaging time and thus patient discomfort, indicating that these imaging parameters are highly interdependent to each other (Plenge et al., 2012).

Image super-resolution (SR) provides an effective alternative to enhance the resolution of MR images from the perspective of postprocessing (Zhao et al., 2018c), which aims at recovering a HR image from one or more low-resolution (LR) images. As a postprocessing method, image SR is an active research field that can substantially break through the limitations of hardware device and improve image resolution (Park et al., 2003; Plenge et al., 2012). In recent years, deep learning techniques (LeCun et al., 2015), especially convolutional neural networks (CNNs) (LeCun et al., 1989), have greatly promoted the development of this field, resulting in the emergence of many advanced SR methods, such as SRCNN (Dong et al., 2016a), DRCN (Kim et al., 2016b), DRRN (Tai et al., 2017a), MemNet (Tai et al., 2017b), VDSR (Kim et al., 2016a), EDSR/MDSR (Lim et al.), RDN (Zhang et al., 2018b), RCAN (Zhang et al., 2018a) and CSN (Zhao et al., 2018c) etc. Although these models have excellent performance, most of them are mainly aimed at the SR tasks on natural images, instead of MR images.

In medical image processing community, there are also some deep CNN-based medical image SR methods, e.g., Pham et al., Chen et al. (2018b,a), Zhao et al. (2018a,c) etc. The primary intention of these methods, to some extent, is to improve the performance of MR image SR tasks. However, a fundamental consideration in many MRI experiments is how to reduce imaging time to improve patient comfort and avoid motion artifacts as much as possible. Therefore, high-efficiency HR image reconstruction is also of significance in practical applications. On the other hand, an important problem in medical image

* Corresponding author.
E-mail addresses: zxlation@foxmail.com (X. Zhao), tao.zhang@uestc.edu.cn (T. Zhang).

https://doi.org/10.1016/j.cviu.2020.103075
Received 20 November 2019; Received in revised form 10 August 2020; Accepted 19 August 2020
Available online 28 August 2020

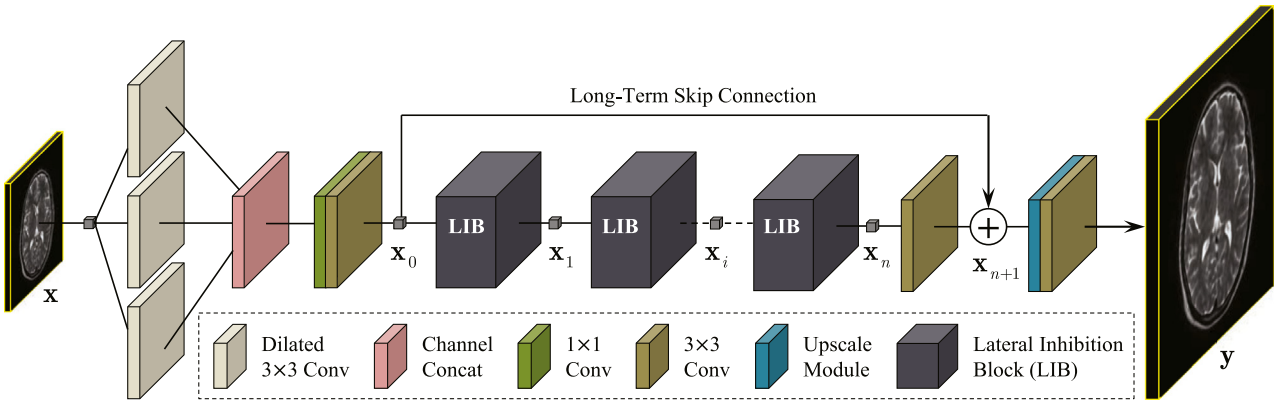

Fig. 1. The overall structure of the proposed lateral inhibition network (LIN). The dilated 3×3 convolutions for feature extraction have different dilation rates to collect image features in the receptive fields with different sizes. These features are then concatenated along the channel direction and integrated together with a 1×1 convolutional layer.

processing with deep learning techniques is the degradation of training samples (Litjens et al., 2017; Zhao et al., 2018c). As the model scale (e.g., model parameters, network depth/width etc.) increases, it will be more difficult to train larger models with these degraded medical training samples (Zhao et al., 2018c, 2019), and more tricks are needed for successful model training (Li et al., 2018). In this regard, lightweight models *may* be more appropriate for practical applications of medical image SR tasks.

With these considerations, we aim at efficient MR image SR reconstruction by introducing a lightweight CNN model in this paper. The proposed model, which we term as lateral inhibition network (LIN), is well-motivated and inspired by the biological lateral inhibition mechanism that assumes there exists explicit inhibitory regulation between adjacent neurons. The building module of our LIN network is local inhibition unit (LIU) that takes residual block (Lim et al.; Zhang et al., 2018b,a) as the backbone and a inhibition tail (IT) is attached to integrate lateral inhibition mechanism into feature mapping. A series of cascaded LIUs construct a local nonlinear mapping block, i.e., lateral inhibition block (LIB), as shown in Fig. 2. Then multiple LIBs are stacked together to build the nonlinear subnet of the proposed LIN model. Besides, to extract shallow features with different receptive field sizes, we use a group of 3×3 dilated conv layers with different dilation rates in the feature extraction subnet, as shown in Fig. 1. Like Lim et al., Zhang et al. (2018b), Zhao et al. (2018c), we only apply one 3×3 conv layer to reconstruct the final output.

Deep CNN models are generally built upon the convolution operation that extracts informative local features by integrating spatial and channel information together within local receptive fields. In fact, a lot of work demonstrates that careful structural design helps to improve the representational capacity of deep models substantially (Simonyan and Zisserman, 2014; He et al., 2016a,b; Kim et al., 2016a; Huang et al., 2017; Hu et al., 2017; Zhao et al., 2018b). The proposed LIU follows this point and serves as a feature regulator that simulates the Hartline–Ratliff equation and explicitly adjusts the hierarchical features of deep models. The explicit adjustment of the hierarchical features is considered beneficial to alleviate the representational burden of deep models and therefore improve SR performance (Hu et al., 2017; Zhao et al., 2018c). The main contributions of this work are as following:

- A lightweight CNN model, LIN, is proposed for efficient and accurate MR image SR tasks. With moderate model parameters and computational overhead, our LIN achieves high-precision and fast SR reconstruction.
- Motivated by the lateral inhibition mechanism, we design a local inhibition unit (LIU) to explicitly impose inhibitory regulation on feature maps, alleviating the representational burden of the model.
- We propose to integrate the shallow features with different receptive field sizes to boost model performance. Through this strategy, we can increase the diversity of the extracted features and provide more effective evidence for nonlinear inference and image reconstruction.
- We experimentally and analytically verify that combining the lateral inhibition mechanism with our shallow feature extraction strategy favors to improving the performance of deep models.

Extensive experiments on various MR images show that our model achieves competitive SR performance with much less model parameters and higher efficiency. The remainder of this paper is organized as follows: in Section 2, we introduce some previous work related to this work. The proposed LIN model is illustrated in Section 3. The experimental results and analyses are given in Section 4, and the conclusion is in Section 5.

2. Related work

2.1. MR image super-resolution

High-resolution medical images provide rich structural and textural details that are critical for accurate postprocessing and early diagnoses. However, HR acquisition based on hardware devices typically decreases image SNR and increases scanning time (Greenspan et al., 2002; Plenge et al., 2012; Shi et al., 2015; Chen et al., 2018b). As an alternative, image SR methods are widely used to enhance the resolution of MR images, and many SR techniques for MR images are studied and proposed in the past decades, such as Greenspan et al. (2001), Shilling et al. (2009) and Peled and Yeshurun (2015) that employ traditional multi-image super-resolution (MISR) to deal with MR image SR tasks, and Rousseau (2008), Manjón et al. (2010a), Rueda et al. (2013) that focus on *single* image super-resolution (SISR) tasks, as well as more advanced methods that are built upon deep CNNs, e.g., Pham et al., Chen et al. (2018b), Zhao et al. (2018c, 2019) etc.

Due to unreasonable assumption or limited representational capacity, early methods for medical image SR usually perform inferiorly and unsatisfactorily. While some methods based on CNNs achieve excellent performance, their models are large in scale and unfriendly to real MRI scene where limited resource is available, e.g., Zhao et al. (2018c, 2019).

2.2. Lateral inhibition mechanism

Lateral inhibition is a neurobiological phenomenon in which a neuron's response to a stimulus is inhibited by the excitation of a neighboring neuron (Rodieck and Stone, 1965; Bakshi and Ghosh, 2017). In neurobiology, lateral inhibition is considered to make neurons more

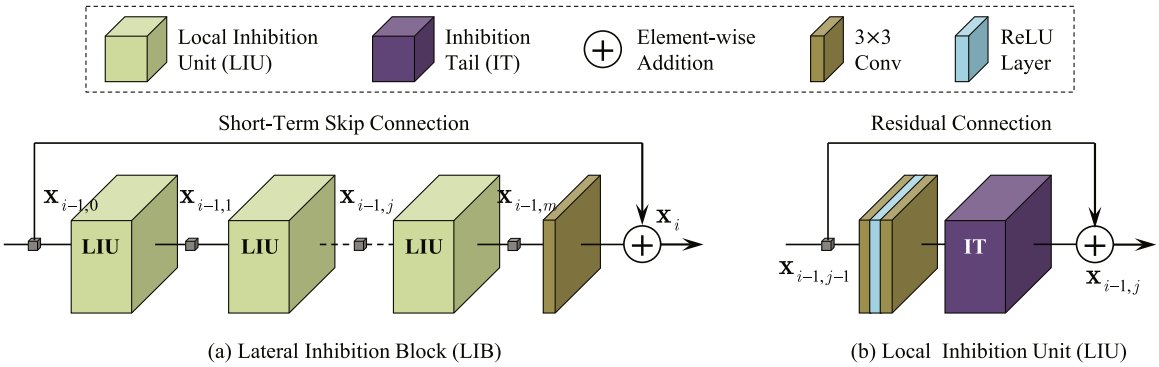

Fig. 2. The internal structure of the building modules of our LIN network. (a) The lateral inhibition block (LIB) consists of a series of local inhibition units (LIU) followed by a 3×3 conv layer. (b) A LIU contains two 3×3 conv layers with a ReLU layer (Nair and Hinton, 2010) in the middle, followed by a inhibition tail (IT) that performs inhibitory regulation.

sensitive to spatially varying of stimulus than to spatially uniform stimulus, thus leading visual neurons more sensitive to nonlinear features. This explicit inhibition of visual features is widely-used in computer vision community to boost the performance of various machine vision tasks, such as image/video segmentation (Fernández-Caballero et al., 2001, 2014), image classification (Fernandes et al., 2013), saliency detection (Cao et al., 2018), face detection (Soares et al., 2014) and image enhancement (Paradis and Jernigan, 1994; Sakamoto and Kato, 1998; Arkachar and Wagh, 2007; Dai et al., 2013; Li et al., 2016) etc.

Lateral inhibition has also been applied in modern artificial neural network (ANN) models. For instance, based on the work developed by Coultrip et al. (1992), Mao and Massaquoi (2007) showed that the lateral inhibition effect from the neighboring neurons in the same layer makes the network more stable and efficient (Fernandes et al., 2013). Arkachar and Wagh (2007) presented a parameterized planer neural network model to study the impact of lateral inhibition on edge enhancement. Another well-known work that involves lateral inhibition mechanism is AlexNet (Krizhevsky et al., 2012), in which a technique called local response normalization (LRN) simulates lateral inhibition and creates competition for big activities.

2.3. Lightweight SR models

After the pioneering work presented by Dong et al. (2016a), the CNN-based SR models show the mainstream trend of building deeper and larger networks for better model performance. Up to now, two representative large-scale models are EDSR (Lim et al.) and RCAN (Zhang et al., 2018a) with network depth of over 160 and 400 layers, and parameters of about 43M and 16M respectively. Despite the excellent SR performance of large-scale models, their practical application and deployment are constrained by the large number of model parameters and computing overhead. When resource-limited MRI is taken into consideration, this is the case.

Subsequently, some lightweight CNN models have also been proposed, such as VDSR (Kim et al., 2016a), AWSRN (Wang et al., 2019), CARN (Ahn et al., 2018), DRRN (Tai et al., 2017a) and IDN (Hui et al., 2018) etc. In addition, there are some lightweight SR models specializing in MR image SR tasks, e.g., RecNet (Hyun et al., 2017) and FSCWRN (Shi et al., 2019). All these methods suggest that lightweight SR models can achieve better trade-off between model performance and scale. In this work, we improve this trade-off for single MR image SR tasks by introducing a lightweight CNN model that is motivated by the lateral inhibition mechanism. We term the proposed model as lateral inhibition network (LIN).

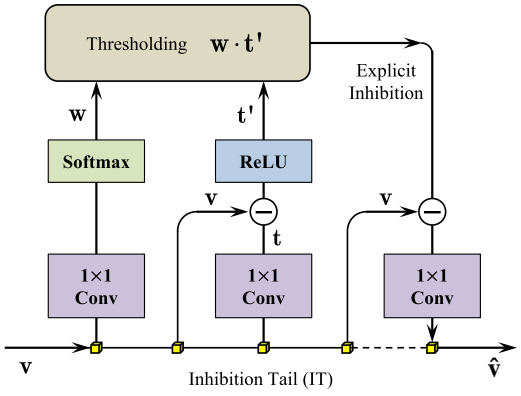

Fig. 3. Computing schema of a inhibition tail. The first bottom-up branch imitates the weight tensor $\mathbf{w}$ of Hartline–Ratliff Equation, and the second bottom-up branch simulates the threshold $\mathbf{t}$. This structure within a LIU acts as an inhibitory regulator of intermediate features.

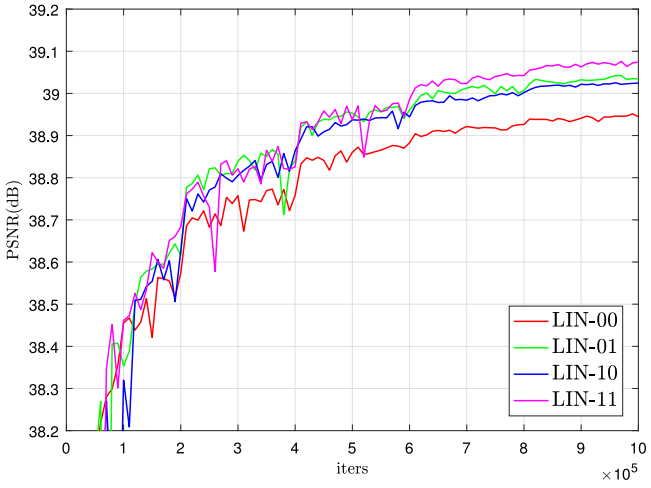

Fig. 4. The validation curves of different configurations of the network on V(PD, BD) with SR×2. The corresponding testing results on T(PD, BD) are shown in Table 1.

3. Lateral inhibition network

3.1. Motivation: Visual inhibition

In neurobiology, lateral inhibition refers to the phenomenon where the excitation of a neuron in a neural network inhibits the response of its neighbors, thus creating a competition between neurons (Rodieck

Table 1
Ablation study on the components of the network structure. The maximum values are marked in red and the second ones are marked in blue (PSNR (dB)/SSIM).

	FE	0	1	0	1
	IT	0	0	1	1
×2	PSNR	40.75	40.81	40.78	40.86
	SSIM	0.9880	0.9882	0.9881	0.9884

Table 2
The impact of n and m on model performance. The evaluation is performed on T(T1, TD) with SR×2.

$n\backslash m$	2	3	4
1	37.30 / 0.9740	37.56 / 0.9752	37.73 / 0.9764
2	37.70 / 0.9759	37.91 / 0.9773	38.04 / 0.9787
3	37.93 / 0.9777	38.01 / 0.9783	38.15 / 0.9791
4	38.00 / 0.9780	38.13 / 0.9790	38.21 / 0.9793

and Stone, 1965; Arkachar and Wagh, 2007; Bakshi and Ghosh, 2017). It mainly occurs in visual processes and makes visual neurons more sensitive to nonlinear features in the scene (Bakshi and Ghosh, 2017). A famous computing model for simulating this visual inhibition is the Hartline–Ratliff Equation (Hartline and Ratliff, 1974):

$$\hat{v}_i = v_i - \sum_{j \neq i} w_{i,j} \cdot \max\left(0; v_j - t_{i,j}\right) \tag{1}$$

where $\hat{v}_i$ is the ith element of the adjusted feature map $\hat{\mathbf{v}}$, v_i is the ith element of the input feature map $\mathbf{v}$. $w_{i,j}$ is the inhibition coefficient of the jth neuron on the ith neuron, and $t_{i,j}$ denotes the threshold that the jth neuron must reach to inhibit the ith neuron. As previously stated, this explicit regulation of features is considered to help alleviate the representational burden of the model and improve the model performance. The proposed LIN model is inspired by this visual inhibition mechanism, and the computation of Eq. (1) is explicitly approximated by the feature regulator IT.

It is worth noting that the Hartline–Ratliff Equation in Eq. (1) requires a nonlocal weighting, resulting in a substantial increase in computing effort. For simplicity, we use ordinary conv layers to substitute the nonlocal weighting.

3.2. Overall network structure

The overall structure of the proposed LIN model is outlined in Figs. 1 and 2. The feature extraction is composed of a set of parallel dilated 3 × 3 conv layers followed by a 1 × 1 conv and a 3 × 3 conv layer. The results of these dilation convolutions are concatenated together along the channel direction. This process can be formally represented as:

$$\mathbf{x}_0 = F_{\text{ext}}(\mathbf{x}), \tag{2}$$

where $\mathbf{x}_0$ represents the extracted shallow feature and $\mathbf{x}$ denotes the input image. $F_{\text{ext}}(\cdot)$ implies the function corresponding to the entire feature extraction process. Next, $\mathbf{x}_0$ is fed into a series of cascaded lateral inhibition blocks (LIBs), which constitute the nonlinear mapping process:

$$\mathbf{x}_n = F_b^n(\mathbf{x}_{n-1}) = F_b^n(F_b^{n-1}(\cdots F_b^1(\mathbf{x}_0)\cdots)), \tag{3}$$

where $\mathbf{x}_i$ is the output of the ith LIB, and the input feature of the $(i+1)$-th LIB. Function $F_b^i(\cdot)$ corresponds to the mapping process of the ith LIB. n indicates the total number of LIBs in the network. At last, a 3 × 3 convolutional layer is employed to collect deep features and a long-term skip connection is used to conduct residual learning:

$$\mathbf{x}_{n+1} = T(\mathbf{x}_n) + \mathbf{x}_0, \tag{4}$$

where $\mathbf{x}_{n+1}$ indicates the collected deep feature and $T(\cdot)$ denotes the 3 × 3 conv layer after $\mathbf{x}_n$, as shown in Fig. 1.

The image reconstruction subnet of the proposed LIN model consists of a upscale module, and usually followed by a 3 × 3 conv layer. This is the same as several typical SR models, such as EDSR (Lim et al.), RDN (Zhang et al., 2018b) and CSN (Zhao et al., 2018c) etc.

3.3. Lateral inhibition block

The structure of LIB and LIU is shown in Fig. 2. Let $\mathbf{x}_{i-1,0} = \mathbf{x}_{i-1}$ be the input of the ith LIB. The mapping process of a LIB can also be iteratively represented as:

$$\mathbf{x}_{i-1,m} = F_u^m(\mathbf{x}_{i-1,m-1}) = F_u^m(F_u^{m-1}(\cdots F_u^1(\mathbf{x}_{i-1,0})\cdots)), \tag{5}$$

where m denotes the number of LIUs in each LIB, and function $F_u^j(\cdot)$ is the mapping of the jth LIU. Finally, a 3 × 3 conv layer is used to produce the final output of the ith LIB, i.e., $\mathbf{x}_i$, as shown in Fig. 2(a). The process can be formalized as:

$$\mathbf{x}_i = R(\mathbf{x}_{i-1,m}) + \mathbf{x}_{i-1,0} = R(\mathbf{x}_{i-1,m}) + \mathbf{x}_{i-1}, \tag{6}$$

where $R(\cdot)$ corresponds to the mapping of the conv layer at the end. In each LIU, lateral inhibition is explicitly implemented by the feature regulator IT (see Figs. 2(b) and 3), which we will illustrate in Section 3.4.

3.4. Inhibition tail

The detailed computing schema of the feature regulator IT is shown in Fig. 3. The first bottom-up branch simulates the weight $\mathbf{w}$ of Eq. (1), and the second bottom-up branch calculates the threshold $\mathbf{t}$. For the branch of $\mathbf{t}$,

$$\mathbf{t}' = \max\left(0; \mathbf{v} - \mathbf{t}\right) = \max\left[0; \mathbf{v} - F_t(\mathbf{v})\right], \tag{7}$$

where $\mathbf{t} = F_t(\mathbf{v})$ is the threshold tensor, and $F_t(\cdot)$ denotes the 1 × 1 conv layer in the second bottom-up branch. For the branch of weighting tensor $\mathbf{w}$,

$$\mathbf{w} = \sigma\left[F_w(\mathbf{v})\right], \tag{8}$$

where $\sigma(\cdot)$ denotes a softmax function that is used to normalize the weight tensor, and $F_w(\cdot)$ corresponds to the 1 × 1 convolution in the first bottom-up branch. Finally, the adjusted hierarchical feature can be obtained by:

$$\hat{\mathbf{v}} = F(\mathbf{v} - \mathbf{w} \otimes \mathbf{t}'), \tag{9}$$

where $F(\cdot)$ corresponds to the last 1 × 1 convolution in Fig. 3 and $\otimes$ denotes the element-wise multiplication. As can be seen, we use ordinary 1 × 1 convolutional operations instead of nonlocal weighting to avoid large computational overhead.

4. Experiments

4.1. Dataset

In this paper, the dataset used in the experiments is the same as that used in CSN (Zhao et al., 2018c), which is derived from the IXI dataset.[1] It contains three typical MR image types: proton density (PD) images, T1-weighted images and T2-weighted images. For each image type, there are 500, 70 and 6 volumes of size 240 × 240 × 96 (height×width×depth) for training, testing and validation, respectively. Besides, two image degradations are also included in this dataset, namely, bicubic downsampling (BD) and k-space truncation (TD). For convenience, we follow the convention descried in Zhao et al. (2018c) to indicate each subdataset. For instance, D(PD, BD) implies the PD

[1] http://brain-development.org/ixi-dataset/.

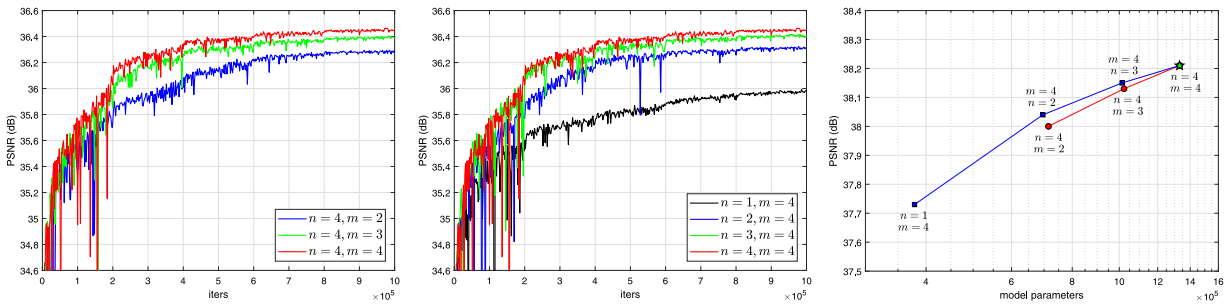

(a) Valid curves ($n = 4$) (b) Valid curves ($m = 4$) (c) Testing results of (a) and (b)

Fig. 5. The performance comparison between LIN models with different number of LIB and LIU. The evaluation is performed on T1 images with k-space truncation degradation (TD) and SR×2. (a) Valid curves when $n = 4, m = 2, 3, 4$. (b) Valid curves when $n = 1, 2, 3, 4, m = 4$. (c) The corresponding testing results of (a) and (b). Model parameters are also shown for clearer comparison.

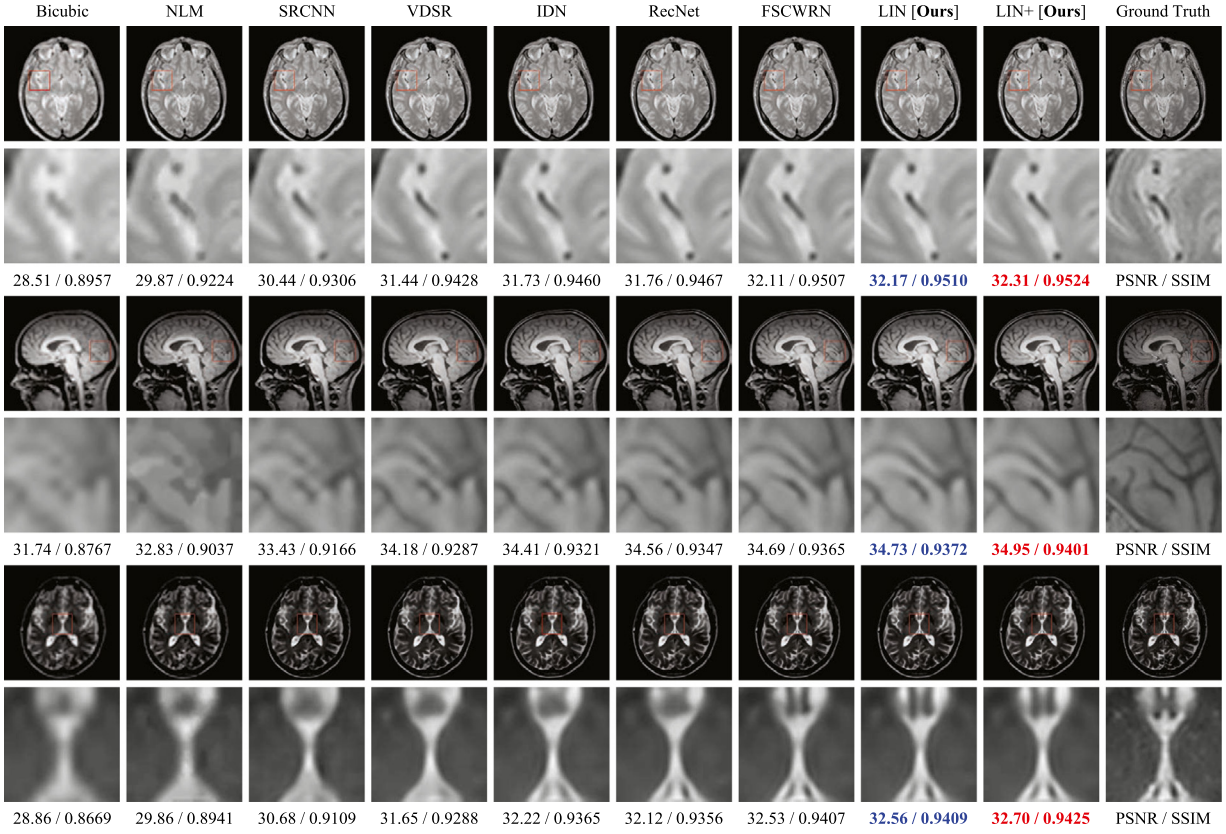

Fig. 6. The visual comparison of several typical lightweight SR models on a PD image (top), T1 image (middle) and T2 image (bottom) with scaling factor = 3, 4, 4, respectively. Image degradation is bicubic-downsampling (BD).

training set (D) under bicubic downsampling, while V(T1, TD) represents the T1 validation set (V) under k-space truncation degradation and T(T2, BD) denotes the testing set (T) of T2 images with bicubic-downsampling degradation.

Note that although the data is in 3D space, this work focuses on 2D image SR. Therefore, in the experiments, we divide 3D volumes into a bunch of slices along the imaging plane and all compared methods deal with 3D volumes slice by slice.

4.2. Implementation details

We set $n = m = 4$ for our finalized LIN model. The number of channels for the two conv layers in each LIU is 128 and 32 respectively. Elsewhere, it is set to 32 except for the final output layer. Mini-batch size is set to be 16. The models are trained with LR image patches of size 24×24 randomly extracted from 2D MR slices with the corresponding HR patches. The training data is augmented by random horizontal and vertical flips, and 90° rotations (transposition).

All models are implemented in TensorFlow 1.9.0 and trained on a NVIDIA GeForce GTX 1080 Ti GPU for 10^6 iterations in total. We use Xavier's method (Glorot and Bengio, 2010) to initialize all model parameters and Adam optimizer (Kingma and Ba, 2014) to minimize the loss by setting $\beta_1 = 0.9$, $\beta_2 = 0.999$ and $\epsilon = 10^{-8}$. Learning rate is initialized as 2×10^{-4} for all layers and halved at every 2×10^5 iterations.

4.3. Model analysis

4.3.1. Ablation investigation

In this section, we investigate the influence of the structural components of the network on the SR performance, including the feature extraction (FE) part and the feature regulator IT. We keep the backbone of the network unchanged and just adjust FE and IT accordingly. For

Table 3
Quantitative comparison between several typical SR models. The maximum values in each comparative cell are marked in red and the second ones are marked in blue. Both degradations (BD and TD) are included here (PSNR (dB) / SSIM).

Mode	Methods	Scale	Params	MultiAdds	PD	T1	T2
BD	Bicubic [2D]	×2	N/A	N/A	35.04 / 0.9664	33.80 / 0.9525	33.44 / 0.9589
	NLM [(Manjón et al., 2010b)]	×2	N/A	N/A	37.26 / 0.9773	35.80 / 0.9685	35.58 / 0.9722
	SRCNN [(Dong et al., 2016a)]	×2	24.5K	52.7G	38.96 / 0.9836	37.12 / 0.9761	37.32 / 0.9796
	VDSR [(Kim et al., 2016a)]	×2	0.67M	612.6G	39.97 / 0.9861	37.67 / 0.9783	38.65 / 0.9836
	IDN [(Hui et al., 2018)]	×2	0.73M	170.8G	40.27 / 0.9869	37.79 / 0.9787	39.09 / 0.9846
	RecNet [(Hyun et al., 2017)]	×2	1.33M	275.0G	40.43 / 0.9873	37.86 / 0.9792	39.13 / 0.9848
	FSCWRN [(Shi et al., 2019)]	×2	3.50M	1170.0G	40.72 / 0.9880	37.98 / 0.9797	39.44 / 0.9855
	The proposed LIN [Ours]	×2	1.33M	306.2G	40.86 / 0.9884	38.04 / 0.9798	39.50 / 0.9856
	The proposed LIN+ [Ours]	×2	1.33M	306.2G	41.03 / 0.9886	38.19 / 0.9803	39.62 / 0.9860
	Bicubic [2D]	×3	N/A	N/A	31.20 / 0.9230	30.15 / 0.8900	29.80 / 0.9093
	NLM [(Manjón et al., 2010b)]	×3	N/A	N/A	32.81 / 0.9436	31.74 / 0.9216	31.28 / 0.9330
	SRCNN [(Dong et al., 2016a)]	×3	24.5K	52.7G	33.60 / 0.9516	32.17 / 0.9276	32.20 / 0.9440
	VDSR [(Kim et al., 2016a)]	×3	0.67M	612.6G	34.66 / 0.9599	32.91 / 0.9378	33.47 / 0.9559
	IDN [(Hui et al., 2018)]	×3	0.83M	76.8G	34.96 / 0.9619	33.06 / 0.9394	33.92 / 0.9591
	RecNet [(Hyun et al., 2017)]	×3	1.33M	275.0G	34.96 / 0.9623	33.05 / 0.9399	33.85 / 0.9588
	FSCWRN [(Shi et al., 2019)]	×3	3.50M	523.5G	35.37 / 0.9653	33.24 / 0.9423	34.27 / 0.9618
	The proposed LIN [Ours]	×3	1.37M	141.2G	35.39 / 0.9654	33.23 / 0.9421	34.26 / 0.9616
	The proposed LIN+ [Ours]	×3	1.37M	141.2G	35.56 / 0.9661	33.44 / 0.9440	34.41 / 0.9627
	Bicubic [2D]	×4	N/A	N/A	29.13 / 0.8799	28.28 / 0.8312	27.86 / 0.8611
	NLM [(Manjón et al., 2010b)]	×4	N/A	N/A	30.27 / 0.9044	29.31 / 0.8655	28.85 / 0.8875
	SRCNN [(Dong et al., 2016a)]	×4	24.5K	52.7G	31.10 / 0.9181	29.90 / 0.8796	29.69 / 0.9052
	VDSR [(Kim et al., 2016a)]	×4	0.67M	612.6G	32.09 / 0.9311	30.57 / 0.8932	30.79 / 0.9240
	IDN [(Hui et al., 2018)]	×4	0.96M	43.9G	32.47 / 0.9354	30.74 / 0.8966	31.37 / 0.9312
	RecNet [(Hyun et al., 2017)]	×4	1.33M	275.0G	32.58 / 0.9378	30.86 / 0.9005	31.30 / 0.9310
	FSCWRN [(Shi et al., 2019)]	×4	3.50M	297.3G	32.91 / 0.9415	30.96 / 0.9022	31.71 / 0.9359
	The proposed LIN [Ours]	×4	1.36M	85.6G	32.94 / 0.9417	31.01 / 0.9033	31.72 / 0.9361
	The proposed LIN+ [Ours]	×4	1.36M	85.6G	33.12 / 0.9432	31.28 / 0.9073	31.88 / 0.9376
TD	Bicubic [2D]	×2	N/A	N/A	34.65 / 0.9625	33.38 / 0.9460	33.06 / 0.9541
	NLM [(Manjón et al., 2010b)]	×2	N/A	N/A	36.18 / 0.9707	34.71 / 0.9581	34.56 / 0.9641
	SRCNN [(Dong et al., 2016a)]	×2	24.5K	52.7G	38.23 / 0.9802	36.52 / 0.9705	37.04 / 0.9773
	VDSR [(Kim et al., 2016a)]	×2	0.67M	612.6G	39.89 / 0.9850	37.58 / 0.9760	38.74 / 0.9823
	IDN [(Hui et al., 2018)]	×2	0.73M	170.8G	40.43 / 0.9862	37.79 / 0.9765	39.48 / 0.9842
	RecNet [(Hyun et al., 2017)]	×2	1.33M	275.0G	40.10 / 0.9857	37.54 / 0.9764	39.03 / 0.9832
	FSCWRN [(Shi et al., 2019)]	×2	3.50M	1170.0G	40.91 / 0.9876	38.04 / 0.9786	39.82 / 0.9851
	The proposed LIN [Ours]	×2	1.33M	306.2G	41.11 / 0.9880	38.21 / 0.9793	40.02 / 0.9855
	The proposed LIN+ [Ours]	×2	1.33M	306.2G	41.31 / 0.9886	38.40 / 0.9801	40.18 / 0.9859
	Bicubic [2D]	×3	N/A	N/A	30.88 / 0.9167	29.79 / 0.8793	29.50 / 0.9016
	NLM [(Manjón et al., 2010b)]	×3	N/A	N/A	32.02 / 0.9324	30.83 / 0.9027	30.57 / 0.9197
	SRCNN [(Dong et al., 2016a)]	×3	24.5K	52.7G	32.90 / 0.9432	31.72 / 0.9187	31.80 / 0.9381
	VDSR [(Kim et al., 2016a)]	×3	0.67M	612.6G	34.27 / 0.9555	32.57 / 0.9304	33.23 / 0.9515
	IDN [(Hui et al., 2018)]	×3	0.83M	76.8G	34.88 / 0.9598	32.86 / 0.9348	33.95 / 0.9569
	RecNet [(Hyun et al., 2017)]	×3	1.33M	275.0G	34.67 / 0.9590	32.80 / 0.9347	33.69 / 0.9554
	FSCWRN [(Shi et al., 2019)]	×3	3.50M	523.5G	35.30 / 0.9636	33.09 / 0.9390	34.34 / 0.9603
	The proposed LIN [Ours]	×3	1.37M	141.2G	35.39 / 0.9642	33.25 / 0.9406	34.45 / 0.9609
	The proposed LIN+ [Ours]	×3	1.37M	141.2G	35.59 / 0.9656	33.50 / 0.9429	34.63 / 0.9622
	Bicubic [2D]	×4	N/A	N/A	28.82 / 0.8713	27.96 / 0.8182	27.60 / 0.8511
	NLM [(Manjón et al., 2010b)]	×4	N/A	N/A	29.27 / 0.8906	28.68 / 0.8439	28.37 / 0.8718
	SRCNN [(Dong et al., 2016a)]	×4	24.5K	52.7G	30.52 / 0.9078	29.31 / 0.8616	29.32 / 0.8960
	VDSR [(Kim et al., 2016a)]	×4	0.67M	612.6G	31.69 / 0.9244	30.14 / 0.8818	30.51 / 0.9162
	IDN [(Hui et al., 2018)]	×4	0.96M	43.9G	32.33 / 0.9318	30.40 / 0.8889	31.31 / 0.9270
	RecNet [(Hyun et al., 2017)]	×4	1.33M	275.0G	32.16 / 0.9310	30.46 / 0.8900	31.03 / 0.9243
	FSCWRN [(Shi et al., 2019)]	×4	3.50M	297.3G	32.78 / 0.9387	30.79 / 0.8973	31.71 / 0.9334
	The proposed LIN [Ours]	×4	1.36M	85.6G	32.82 / 0.9391	30.88 / 0.8990	31.77 / 0.9339
	The proposed LIN+ [Ours]	×4	1.36M	85.6G	33.03 / 0.9415	31.20 / 0.9041	31.96 / 0.9362

FE, the comparative case is a single 3 × 3 conv layer that is denoted as "0", and a group of dilated 3 × 3 conv layers used by the proposed LIN model is denoted as "1". For IT, the comparative case is removing the IT from the LIU, also denoted as "0". And LIU attached by the IT is denoted as "1", as shown in Fig. 4 and Table 1. The evaluation is performed on the testing dataset of PD images with SR×2 and bicubic-downsampling, i.e., T(PD, BD).

As can be seen from Table 1, the baseline network structure without FE and IT (LIN-00) gives PSNR = 40.75dB and SSIM = 0.9880. However, by adding either FE or IT into this baseline architecture, the performance is simply improved. Although FE seems to contribute more to performance gain than IT, we can see that the co-occurrence of FE and IT within the network can further boost the performance (LIN-11). We also visualize the convergence curves of these different network configurations in Fig. 4, which are in line with the previous analyses on the testing results. These comparisons and analyses imply that the parallel feature extraction and the inhibitory regulation of intermediate features help the model to improve the representational capacity and obtain better SR performance.

4.3.2. Impact of n and m

We also analysis the impact of the number of LIB and LIU on the performance of the model. First, we fix n at 4 and set $m = 2, 3, 4$. Fig. 5(a) shows the valid curves of these models on V(T1, TD) with SR×2. Also, we fix $m = 4$ and set $n = 1, 2, 3, 4$. The valid curves are shown in Fig. 5(b) in this case. As we can see, the model performance improves as n or m increases, which is unsurprising because the increase in n and m typically enlarge model scale, e.g., network depth and/or model parameters. The testing results corresponding to these valid results are shown in Fig. 5(c) versus their model parameters.

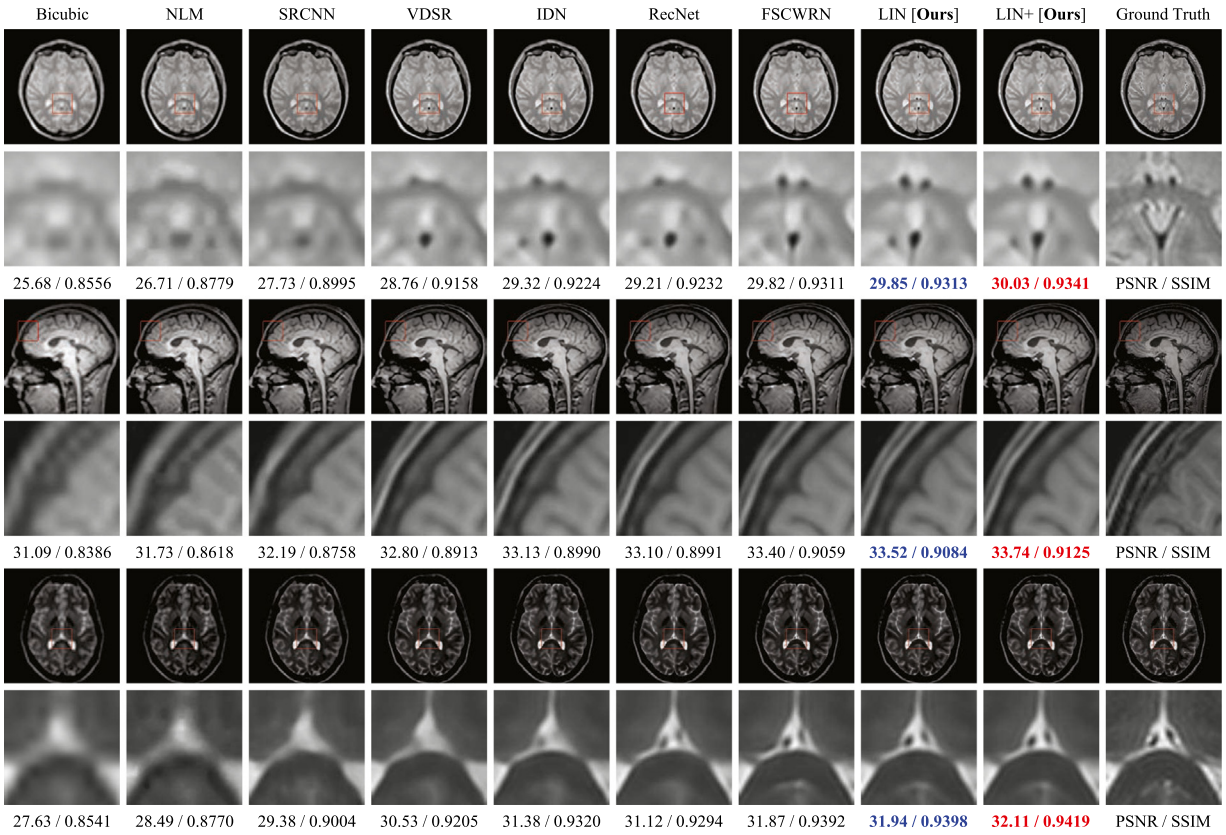

Fig. 7. The visual comparison of several typical lightweight SR models on a PD image (top), T1 image (middle), and T2 image (bottom) with scaling factor = 4. Image degradation is k-space truncation (TD).

An obvious observation is that when $2 < n, m < 4$, the configuration with $n = 2, m = 4$ performs better than that with $n = 4, m = 2$, and $n = 3, m = 4$ performs better than $n = 4, m = 3$ (less model parameters and higher PSNR). However, the advantage decreases gradually as n and m increase.

To further exhibit the impact of n and m, several other models with different n and m are evaluated, and the results are shown in Table 2, where similar results can also be observed.

4.4. Comparison with other methods

We illustrate the effectiveness of the proposed LIN model by comparing it with several typical SR methods quantitatively and qualitatively: (1) NLM (Manjón et al., 2010b) specifically for MRI upsampling; (2) SRCNN (Dong et al., 2016a), IDN (Hui et al., 2018) and VDSR (Kim et al., 2016a) for natural images; (3) RecNet (Hyun et al., 2017) and FSCWRN (Shi et al., 2019) specifically for MR image SR. The quantitative results of these methods are directly cited from Zhao et al. (2019), including the peak signal to noise ratio (PSNR) and structural similarity index measurement (SSIM) (Wang et al., 2004). Note that we only compare the models that have roughly similar number of parameters as our LIN model. For fair comparison, we follow the setting of hyper-parameters in Zhao et al. (2019), like batch size, patch size and training steps etc. Besides, we also adopt the trick of geometric self-ensemble (Lim et al.) to further improve the performance of the model, and in this case it is denoted as LIN+ (as shown in Table 3).

For evaluating lightweight models, the computing overhead is also an important factor to consider. To this end, we introduce Multi-Adds (Ahn et al., 2018) as a performance index to evaluate the computational consumption of the model:

$$\text{MultiAdds} = k \times k \times C_{in} \times C_{out} \times H \times W, \tag{10}$$

where k is the size of conv kernels, and C_{in} and C_{out} denote the input and output channels. H and W represent the spatial size of output features. The size of HR images is assumed to be 720p i.e., 1280×720, for the calculation of MultAdds, as in Ahn et al. (2018) and Wang et al. (2019).

4.4.1. Quantitative evaluation

Table 3 shows the quantitative comparison of these methods as well as their model scales. Overall, as can be observed, our LIN model achieves the best SR performance although it has more moderate model parameters, almost the same as RecNet (Hyun et al., 2017). The network parameters of FSCWRN (Shi et al., 2019) are about 2.6 times that of ours, but our LIN model still performs better. In case of TD, our LIN models move beyond other methods in terms of all comparative cases. This may indicate that the proposed LIN models are more suitable for lightweight MR image SR tasks in that k-space truncation degradation aims to simulate the image acquisition process in real-world MRI (Zhao et al., 2018c). Furthermore, we can see from Table 3 that the enhanced version LIN+ gives obviously better SR performance than the original LIN although they have the same model scale, illustrating the effectiveness of geometric self-ensemble strategy in single MR image SR tasks.

Different from other methods, the proposed models conduct the nonlinear inference in LR image space (Dong et al., 2016b; Lim et al.; Zhang et al., 2018b; Zhao et al., 2018c) and upscale the input LR image in image reconstruction phase, and the model scale of our LIN models therefore varies slightly with the scaling factor, as shown in Table 3. Nevertheless, both LIN and LIN+ still provide the best tradeoff between network scale and SR performance. For example, the best model in Table 3 is FSCWRN (Shi et al., 2019) except the proposed models. While our LIN only takes up less than 40% of its parameters, and less than 30% of its computing overhead.

Table 4
Running time of the compared models to process a single volume (seconds / volume).

scale	Bicubic	NLM	SRCNN	VDSR	IDN	RecNet	FSCWRN	LIN
$r = 2$	0.1543	90.4238	0.3021	1.7644	0.8123	0.8231	2.1906	0.8501
$r = 3$	0.1578	63.5357	0.3211	2.6488	0.4415	0.9652	1.1403	0.9689
$r = 4$	0.1610	46.0358	0.3284	2.4131	0.2773	1.0277	0.7477	1.0788

4.4.2. Visual comparison

Fig. 6 displays the visual comparison between these methods under bicubic-downsampling degradation. To demonstrate the effectiveness of the proposed models on different types of MR images, we present the visualizations of PD (top), T1 (middle) and T2 (bottom) images respectively. The SR scaling factors for these comparative cases are 3, 4, and 4, respectively. As can be observed from Fig. 6, methods based on CNNs, e.g., SRCNN (Dong et al., 2016a) and VDSR (Kim et al., 2016a), perform significantly better than conventional methods, i.e., Bicubic and NLM (Manjón et al., 2010b). However, the proposed models present the best visual results with clearer details and texture structures. The quantitative metrics below each clipped image also illustrate the accuracy of the proposed models.

Fig. 7 shows the visual results of these methods under k-space truncation degradation (**TD**). The scaling factor is 4 for all these comparative cases. Also, we can see that the proposed LIN and LIN+ models present the best visualization on various types of MR images. For instance, the middle row of Fig. 7 is the visual comparison on a T1 image. The skull and the dark groove on it present the sharpest edges in the results of our models, and the sulcus gyrus in our results most clearly implies its underlying structures. The bottom row in Fig. 7 is the visual results of a T2 image. Most methods fail to recover the black holes in the middle of clipped images. Although they can be recovered by FSCWRN (Shi et al., 2019) and RecNet (Hyun et al., 2017), our results are closer to the ground truth and present more faithful latent structures than other methods.

4.4.3. Running time

Table 4 collects the running time required by the compared methods to process a single volume. The sizes of 3D volumes for $r = 2$, $r = 3$ and $r = 4$ are $120 \times 120 \times 96$, $80 \times 80 \times 96$ and $60 \times 60 \times 96$, respectively. The evaluation is performed with a Omnisky supercomputing workstation equipped with 64GB memory and two Intel Xeon E5-2630 CPUs (2.20 GHz). The methods based on CNNs are evaluated with a single NVIDIA GTX 1080 Ti GPU. Note that the running time is averaged on 3D volumes instead of 2D slices, as medical images are usually organized as 3D volumes.

According to Table 4, the slowest execution is NLM (Manjón et al., 2010b), which is not surprising because it is based on iterative optimization processing. Besides, the running time of deep CNN-based methods is similar, all less than 5 s per volume. The efficiency of our models is comparable to other fast models, e.g., IDN (Hui et al., 2018) and RecNet (Hyun et al., 2017), due to their similar model scales. However, the proposed LIN and LIN+ perform significantly better than these models, as shown in Table 3. This implies that our models are not only highly accurate in SR performance, but also practically useful in real-world applications.

5. Conclusion

We demonstrate a novel CNN model for single MR image SR tasks in this paper, which is motivated by the lateral inhibition mechanism in neurobiology. An inhibition tail that explicitly adjusts the activation of hidden neurons is designed to simulate the Hartline–Ratliff Equation (Hartline and Ratliff, 1974) and used as a regulator of hierarchical features. When the model is lightweight in scale, explicitly imposing inhibitory adjustment on features is considered to help alleviate the representational burden of deep models and improve their SR performance. In addition, we also adopt geometric self-ensemble strategy (Lim et al.) to further improve the performance of the proposed models. Extensive experiments on different MR images exhibit the superiority of the proposed models over other lightweight SR models. Because of the better tradeoff between model scale and performance, our LIN models should be more suitable for real-world applications and deployment.

CRediT authorship contribution statement

Xiaole Zhao: Writing - original draft, Supervision, Investigation, Software, Writing - review & editing. **Xiafei Hu:** Investigation, Software. **Ying Liao:** Writing - original draft, Investigation. **Tian He:** Visualization, Investigation. **Tao Zhang:** Conceptualization, Methodology, Supervision. **Xueming Zou:** Conceptualization, Supervision. **Jinsha Tian:** Formal analysis, Validation, Writing - review & editing.

Declaration of competing interest

The authors declare that they have no known competing financial interests or personal relationships that could have appeared to influence the work reported in this paper.

Acknowledgments

The work is supported in part by Sichuan Science and Technology Program under Grant 2019YJ0181, and National Key Research and Development Program of China under Grant No. 2016YFC0100800 and 2016YFC0100802.

References

Ahn, N., Kang, B., Sohn, K., 2018. Fast, accurate, and lightweight super-resolution with cascading residual network. In: ECCV. pp. 256–272.
Arkachar, P., Wagh, M.D., 2007. Criticality of lateral inhibition for edge enhancement in neural systems. Neurocomputing 70 (4–6), 991–999.
Bakshi, A., Ghosh, K., 2017. A neural model of attention and feedback for computing perceived brightness in vision. Handbook of Neural Computation. pp. 487–513.
Cao, C., Huang, Y., Wang, Z., Wang, L., Xu, N., Tan, T., 2018. Lateral inhibition-inspired convolutional neural network for visual attention and saliency detection. In: AAAI. pp. 6690–6697.
Chen, Y., Shi, F., Christodoulou, A.G., et al., 2018a. Efficient and accurate MRI super-resolution using a generative adversarial network and 3D multi-level densely connected network. In: MICCAI 2018. pp. 91–99.
Chen, Y., Xie, Y., Zhou, Z., et al., 2018b. Brain MRI super resolution using 3D deep densely connected neural networks. In: 15th IEEE International Symposium on Biomedical Imaging, ISBI 2018, pp. 739–742.
Coultrip, R.L., Granger, R.H., Lynch, G., 1992. A cortical model of winner-take-all competition via lateral inhibition. Neural Netw. 5 (1), 47–54.
Dai, S., Du, Z., Zhang, Y., Hu, Y., 2013. Edge enhancement using adaptive lateral inhibition. In: ICCSNT. pp. 1133–1137.
Dong, C., Loy, C.C., He, K., Tang, X., 2016a. Image super-resolution using deep convolutional networks. IEEE TPAMI 38 (2), 295–307.
Dong, C., Loy, C.C., Tang, X., 2016b. Accelerating the super-resolution convolutional neural network. In: ECCV. pp. 391–407.
Fernandes, B.J.T., Cavalcanti, G.D.C., Ren, T.I., 2013. Lateral inhibition pyramidal neural network for image classification. IEEE Trans. Cybern. 43 (6), 2082–2092.
Fernández-Caballero, A., López, M.T., Serrano-Cuerda, J., Carlos Castillo, J., 2014. Color video segmentation by lateral inhibition in accumulative computation. Signal Image Video Process. 8 (6), 1179–1188.
Fernández-Caballero, A., Mira, J., Fernández, M.A., López, M.T., 2001. Segmentation from motion of non-rigid objects by neuronal lateral interaction. Pattern Recognit. Lett. 22 (14), 1517–1524.
Glorot, X., Bengio, Y., 2010. Understanding the difficulty of training deep feedforward neural networks. In: AISTATS 2010. pp. 249–256.
Greenspan, H., Oz, G., Kiryati, N., Peled, S., 2002. Super-resolution in MRI. In: ISBI. pp. 943–946.

Greenspan, H., Peled, S., Oz, G., Kiryati, N., 2001. MRI inter-slice reconstruction using super-resolution. In: MICCAI 2001. pp. 1204–1206.
Hartline, H., Ratliff, F., 1974. Studies on Excitation and Inhibition in the Retina. The Rockefeller University Press, New York.
He, K., Zhang, X., Ren, S., Sun, J., 2016a. Deep residual learning for image recognition. In: CVPR. pp. 770–778.
He, K., Zhang, X., Ren, S., Sun, J., 2016b. Identity mappings in deep residual networks. In: ECCV. pp. 630–645.
Hu, J., Shen, L., Albanie, S., Sun, G., Wu, E., 2017. Squeeze-and-excitation networks. ArXiv preprint arXiv:1709.01507.
Huang, G., Liu, Z., et al., 2017. Densely connected convolutional networks. In: CVPR. pp. 2261–2269.
Hui, Z., Wang, X., Gao, X., 2018. Fast and accurate single image super-resolution via information distillation network. In: CVPR. pp. 723–731.
Hyun, C.M., Kim, H.P., Lee, S.M., et al., 2017. Deep learning for undersampled MRI reconstruction. ArXiv preprint arXiv:1709.02576.
Kim, J., Lee, J.K., Lee, K.M., 2016a. Accurate image super-resolution using very deep convolutional networks. In: CVPR 2016. pp. 1646–1654.
Kim, J., Lee, J.K., Lee, K.M., 2016b. Deeply-recursive convolutional network for image super-resolution. In: CVPR 2016. pp. 1637–1645.
Kingma, D.P., Ba, J., 2014. Adam: A method for stochastic optimization. arXiv preprint arxiv:1412.6980.
Krizhevsky, A., Sutskever, I., Hinton, G.E., 2012. Imagenet classification with deep convolutional neural networks. In: NIPS. pp. 1106–1114.
LeCun, Y., Bengio, Y., Hinton, G., 2015. Deep learning. Nature 521 (7553), 436–444.
LeCun, Y., Boser, B.E., et al., 1989. Backpropagation applied to handwritten zip code recognition. Neural Comput. 1 (4), 541–551.
Li, J., Fang, F., Mei, K., Zhang, G., 2018. Multi-scale residual network for image super-resolution. In: ECCV. pp. 527–542.
Li, B., Li, Y., Cao, H., Salimi, H., 2016. Image enhancement via lateral inhibition: An analysis under illumination changes. Optik 127 (12), 5078–5083.
Lim, B., Son, S., Kim, H., Nah, S., Lee, K.M., 2017. Enhanced deep residual networks for single image super-resolution. In: CVPR Workshops 2017, pp. 1132–1140.
Litjens, G., Kooi, T., et al., 2017. A survey on deep learning in medical image analysis. Med. Image Anal. 42 (9), 60–88.
Manjón, J.V., Coupé, P., Buades, A., Collins, D.L., Robles, M., 2010a. MRI super-resolution using self-similarity and image priors. Int. J. Biomed. Imaging 2010, 425891.
Manjón, J.V., Coupé, P., Buades, A., et al., 2010b. Non-local MRI upsampling. Med. Image Anal. 14 (6), 784–792.
Mao, Z., Massaquoi, S.G., 2007. Dynamics of winner-take-all competition in recurrent neural networks with lateral inhibition. IEEE Trans. Neural Netw. 18 (1), 55–69.
Nair, V., Hinton, G.E., 2010. Rectified linear units improve restricted Boltzmann machines. In: ICML 2010. pp. 807–814.
Paradis, M.A.K., Jernigan, M.E., 1994. Homomorphic vs. multiplicative lateral inhibition models for image enhancement. In: ICSMC, vol. 1. pp. 286–291.
Park, S.C., Min, K.P., Kang, M.G., 2003. Super-resolution image reconstruction: a technical overview. IEEE Signal Process. Mag. 20 (3), 21–36.
Peled, S., Yeshurun, Y., 2015. Super-resolution in MRI: application to human white matter fiber tract visualization by diffusion tensor imaging. Magn. Reson. Med. 45 (1), 29–35.
Pham, C.H., Ducournau, A., Fablet, R., Rousseau, F., 2017. Brain MRI super-resolution using deep 3D convolutional networks. In: 14th IEEE International Symposium on Biomedical Imaging, ISBI 2017, pp. 197–200.
Plenge, E., Poot, D.H.J., Bernsen, M., et al., 2012. Super-resolution methods in MRI: can they improve the trade-off between resolution, signal-to-noise ratio, and acquisition time? Magn. Reson. Med. 68 (6), 1983–1993.
Reeth, E.V., Tham, I.W., et al., 2012. Super-resolution in magnetic resonance imaging: A review. Concepts Magn. Reson. A 40A (6), 306–325.
Rodieck, R.W., Stone, J., 1965. Analysis of receptive fields of cat retinal ganglion cells. J. Neurophysiol. 28 (5), 832–849.
Rousseau, F., 2008. Brain hallucination. In: ECCV 2008. pp. 497–508.
Rueda, A., Malpica, N., Romero, E., 2013. Single-image super-resolution of brain MR images using over complete dictionaries. MIA 17 (1), 113–132.
Sakamoto, T., Kato, T., 1998. Image enhancement and improvement of both color and brightness contrast based on lateral inhibition method. In: IAPR. pp. 124–131.
Shi, F., Cheng, J., Wang, L., Yap, P.-T., Shen, D., 2015. LRTV: MR image super-resolution with low-rank and total variation regularizations. IEEE Trans. Med. Imaging 34 (12), 2459–2466.
Shi, J., Li, Z., Ying, S., et al., 2019. MR image super-resolution via wide residual networks with fixed skip connection. IEEE J. Biomed. Health Inform. 23 (3), 1129–1140.
Shilling, R.Z., Robbie, T.Q., et al., 2009. A super-resolution framework for 3D high-resolution and high-contrast imaging using 2D multislice MRI. IEEE Trans. Med. Imaging 28 (5), 633–644.
Simonyan, K., Zisserman, A., 2014. Very deep convolutional networks for large-scale image recognition. arXiv preprint arxiv:1409.1556.
Soares, A.M., Fernandes, B.J.T., Bastos-Filho, C.J.A., 2014. Lateral inhibition pyramidal neural networks designed by particle swarm optimization. In: ICANN. pp. 667–674.
Tai, Y., Yang, J., Liu, X., 2017a. Image super-resolution via deep recursive residual network. In: CVPR 2017. pp. 2790–2798.
Tai, Y., Yang, J., Liu, X., Xu, C., 2017b. Memnet: A persistent memory network for image restoration. In: ICCV 2017. pp. 4549–4557.
Wang, Z., Bovik, A.C., Sheikh, H.R., Simoncelli, E.P., 2004. Image quality assessment: from error visibility to structural similarity. IEEE Trans. Image Process. 13 (4), 600–612.
Wang, C., Li, Z., Shi, J., 2019. Lightweight image super-resolution with adaptive weighted learning network. ArXiv preprint arXiv:1904.02358.
Zhang, Y., Li, K., Li, K., et al., 2018a. Image super-resolution using very deep residual channel attention networks. In: ECCV 2018. pp. 294–310.
Zhang, Y., Tian, Y., Kong, Y., Zhong, B., Fu, Y., 2018b. Residual dense network for image super-resolution. In: CVPR 2018. pp. 2472–2481.
Zhao, C., Carass, A., Dewey, B.E., Prince, J.L., 2018a. Self super-resolution for magnetic resonance images using deep networks. In: 15th IEEE International Symposium on Biomedical Imaging, ISBI 2018, pp. 365–368.
Zhao, L., Li, M., et al., 2018b. Deep convolutional neural networks with merge-and-run mappings. In: IJCAI. pp. 3170–3176.
Zhao, X., Zhang, H., Liu, H., Qin, Y., Zhang, T., Zou, X., 2019. Single MR image super-resolution via channel splitting and serial fusion network. ArXiv preprint arXiv:1901.06484.
Zhao, X., Zhang, Y., Zhang, T., Zou, X., 2018c. Channel splitting network for single MR image super-resolution. ArXiv preprint arxiv:1810.06453.